

WORKSHOP ON FAST CHERENKOV DETECTORS - PHOTON DETECTION,  
DIRC DESIGN AND DAQ  
SEPTEMBER 4–6, 2013, GIESSEN, GERMANY

## The CBM-RICH detector

J. Adamczewski,<sup>b</sup> K.-H. Becker,<sup>f</sup> S. Belogurov,<sup>c</sup> N. Boldyreva,<sup>d</sup> A. Chernogorov,<sup>c</sup>  
C. Deveau,<sup>a</sup> V. Dobyrn,<sup>d</sup> M. Dürr,<sup>a</sup> J. Eom,<sup>e</sup> J. Eschke,<sup>b</sup> C. Höhne,<sup>a</sup> K.-H. Kampert,<sup>f</sup>  
V. Kleipa,<sup>b</sup> L. Kochenda,<sup>d</sup> B. Kolb,<sup>b</sup> J. Kopfer,<sup>f</sup> P. Kravtsov,<sup>d</sup> S. Lebedev,<sup>a</sup>  
E. Leonova,<sup>d</sup> E. Lebedeva,<sup>a</sup> S. Linev,<sup>b</sup> T. Mahmoud,<sup>a</sup> J. Michel,<sup>b</sup> N. Miftakhov,<sup>d</sup>  
Y. Nam,<sup>e</sup> W. Niebur,<sup>b</sup> K. Oh,<sup>e</sup> E. Ovcharenko,<sup>c</sup> C. Pauly,<sup>f</sup> J. Pouryamout,<sup>f</sup>  
S. Querschfeld,<sup>f</sup> J. Rautenberg,<sup>f</sup> S. Reinecke,<sup>f,1</sup> Y. Riabov,<sup>d</sup> E. Roshchin,<sup>d</sup>  
V. Samsonov,<sup>d</sup> J. Song,<sup>e</sup> O. Tarasenkova,<sup>d</sup> T. Torres de Heidenreich,<sup>b</sup> M. Traxler,<sup>b</sup>  
C. Ugur,<sup>b</sup> E. Vznuzdaev,<sup>d</sup> M. Vznuzdaev,<sup>d</sup> J. Yi<sup>e</sup> and I.-K. Yoo<sup>e</sup>

<sup>a</sup>Justus-Liebig-Universität Gießen,

Heinrich-Buff-Ring 16, 35392 Giessen, Germany

<sup>b</sup>GSI Helmholtzzentrum für Schwerionenforschung GmbH,

Planckstraße 1, 64291 Darmstadt, Germany

<sup>c</sup>Institute for Theoretical and Experimental Physics (ITEP),

Bolshaya Cheremushkinskaya 25, 117218 Moscow, Russia

<sup>d</sup>Petersburg Nuclear Physics Institute (PNPI), Orlova Roscha,

Gatchina, Leningrad district, 188300, Russia

<sup>e</sup>Pusan National University (PNU),

Busandaehak-ro 63beon-gil, Geumjeong-gu, Busan 609-735, Korea

<sup>f</sup>Bergische Universität Wuppertal, Gaußstraße 20, 42219 Wuppertal, Germany

E-mail: [reinecke@uni-wuppertal.de](mailto:reinecke@uni-wuppertal.de)

**ABSTRACT:** The main task of the future Compressed Baryonic Matter experiment (CBM), to be operated at the FAIR facility at GSI, Darmstadt, is the exploration of the properties of super-dense nuclear matter. The search for in-medium modifications of hadrons, the study of the transition from dense hadronic matter to quark-gluon matter, and the possible location of a critical endpoint in the QCD phase diagram of strongly interacting matter are the most important physics goals of CBM. Detailed measurements of di-leptons stemming from low-mass vector-mesons and charmonium have a large potential to shed light on the existence of such effects.

The Ring Imaging Cherenkov detector of the CBM experiment aims at a clean and efficient electron identification. It is foreseen to use CO<sub>2</sub> as radiator gas and equip the detector with a

<sup>1</sup>Corresponding author.

focussing mirror system and multi-anode photomultiplier tubes as photon detector. In this paper we present selected results of R&D studies and beam test measurements of the detector prototype performed in fall 2011 and 2012 at the CERN/PS with a mixed electron-pion beam.

**KEYWORDS:** Cherenkov detectors; Photon detectors for UV, visible and IR photons (gas)

---

## Contents

<b>1</b>	<b>Introduction</b>	<b>1</b>
<b>2</b>	<b>The RICH concept</b>	<b>2</b>
2.1	Requirements	2
2.2	RICH detector design	2
2.3	Radiator	2
2.4	Mirror system	3
2.5	Photon detector	4
2.6	Wavelength range of accessible photons	5
2.7	Resolution of the Cherenkov angle	5
<b>3</b>	<b>Test results of photon sensor devices</b>	<b>6</b>
3.1	Quantum efficiency of tested MAPMTs and MCPs	6
3.2	QE and reflectivity	8
<b>4</b>	<b>Real size prototype</b>	<b>9</b>
4.1	Prototype concept	9
4.2	Number of hits per ring and ring radius	10
4.3	Comparison of single photon spectra	12
4.4	Performance of MAPMTs/MCPs: Cherenkov ring hit multiplicity	13
4.5	Further detector aspects evaluated in the beam tests	14
<b>5</b>	<b>Conclusion</b>	<b>14</b>

---

## 1 Introduction

The future FAIR facility near Darmstadt will deliver proton and ion beams using two different synchrotron rings, SIS100 and SIS300. SIS100 will be realized first and will deliver a proton beam with energies up to 29 GeV. The ion beams will be 14 (11) AGeV in case of Ca and Au respectively. SIS300 will be realized at a later stage and shall deliver a proton beam with energies up to 90 GeV. The Ca and Au beams will reach an energy of 45 and 35 AGeV respectively [1].

The Compressed Baryonic Matter experiment (CBM) [1] will be one of the main experiments at the FAIR facility. CBM is designed to record proton-proton and nucleus-nucleus collisions at the FAIR beam energies of SIS100 and SIS300. The experiment will study nuclear matter in the regime of highest net-baryon densities ever possible in the lab and explore the QCD phase diagram. Of particular interest are the expected phase transition into a partonic state of matter, the order of such a transition, the possible existence of a critical point and the restoration of chiral symmetry. To study these structures of the QCD phase diagram and to access the properties of dense nuclear

matter a most comprehensive physics program has been established. It covers bulk, charmed, rare, and multi-strange probes. CBM shall achieve efficient measurements of these probes with large acceptance and at high interaction rates.

Among the rare probes are low-mass vector-mesons and charmonium, which can be accessed through their di-leptonic decay modes. Leptons are of special interest in the high multiplicity environment of heavy-ion collisions since they do not interact strongly and leave the hot and dense collision region unaffected. Therefore, their study provides information on the in-medium properties of vector-mesons, as well as on charm production and propagation in hot and dense nuclear matter. Reconstructing the decay leptons requires a set of high performance detectors, among which is the Ring Imaging Cherenkov detector (RICH) that will identify electrons and positrons.

## 2 The RICH concept

### 2.1 Requirements

The CBM-RICH detector is designed to provide electron identification covering the momentum range up to  $p = 8 \text{ GeV}/c$ . The detector has to achieve a pion suppression factor of around 500 allowing for a combined pion suppression with the CBM-Transition Radiation Detector (TRD) of 10000, needed for sufficiently good reconstruction of the di-electron spectra at SIS300.

### 2.2 RICH detector design

In order to accommodate the requirements mentioned above a RICH concept was developed aiming at a stable, robust and fast gaseous detector relying to a large extent on components from industry. The concept foresees a  $\text{CO}_2$  gaseous radiator with focusing mirror elements and a photon detector plane being equipped with Multi-Anode Photomultipliers (MAPMTs) tubes or alternatively with multichannel Microchannel Plates (MCP-PMTs).

The detector will be positioned behind the Silicon Tracking System (STS) detector and the dipole magnet about 1.8 m downstream of the target. The RICH, therefore, faces high track densities and many rings from secondary electrons. Furthermore a significant magnetic stray field is still present right behind the magnet yoke which may influence the photon detection. The first challenge is addressed on the level of ring finding and ring-track matching and the second one requires a reduction of the stray field at the position of the photon detector down to 1 mT if MAPMTs are used. In case such a reduction is impossible, the more expensive MCPs have to be considered.

### 2.3 Radiator

The overall length of the detector is constrained by the maximum distance between the magnet and its shielding yokes (about 1.7 m from target) and the first TRD station which currently is placed at 4.7 m from the target. The number of generated Cherenkov photons is proportional to the radiator length, thus a long RICH detector is always favorable. However, high performance global tracking between STS and TRD limits the place (length) available for the RICH detector. A radiator length of 1.7 m represents a good compromise. With supporting structures the overall length of the RICH detector is 2 m.

Since the RICH detector aims at identifying electrons, a radiator with low refractive index has to be used. This favors gases and we have chosen  $\text{CO}_2$ , which fulfills the requirements within the given length of 1.7 m and has the advantages of being inexpensive and easy to handle. It has a Lorentz factor of  $\gamma_{\text{th}} = 33.3$ , a refractive index of  $n = 1.00045$  ( $T = 0^\circ\text{C}$ ,  $p = 1$  bar), a saturated Cherenkov opening angle of  $\theta_C = 1.72^\circ$ , and a momentum threshold for pions of  $p_{\text{thr}}^\pi = 4.65$  GeV/ $c$  for Cherenkov radiation. With  $\text{CO}_2$  as radiator gas, electrons and pions can be separated up to 8 GeV/ $c$ .

$\text{CO}_2$  is known to show only low scintillation [2]. About 5 scintillation photons per MeV are emitted [2] dominantly in the blue range. In an environment of high particle multiplicity as present in Au-Au collisions and following a conservative estimation of the detector acceptance a total of about 250 additionally measured photons from  $\text{CO}_2$  scintillation are expected. These photons are distributed homogeneously over the photon detector plane and therefore would resemble noise in only 0.45% of all channels. This lies well within the tolerated noise level of the CBM-RICH.

## 2.4 Mirror system

The mirror plane is split horizontally into two arrays of spherical glass mirrors with a reflective  $\text{Al}+\text{MgF}_2$  coating. Their curvature radius is 3 m and their thickness is 6 mm. Glass mirrors are chosen to provide excellent optics combined with a high mechanical stability. Each array is segmented into trapezoidal mirrors of approximately  $40 \times 40$  cm<sup>2</sup> each. In total there will be about 90 segments in both mirror arrays.

Two main properties of the mirrors are essential for the performance of the detector: reflectivity and homogeneity, which affect the number of hits per ring and the ring resolution. Mirrors from three manufacturers *JLO Olomouc*, *Compas*, and *Flabeg* with similar properties and dimensions were tested and characterized in terms of reflectivity and surface homogeneity.

**Reflectivity.** Reflectivity of all mirrors has been measured using a narrow-band spectrometer light source and a calibrated photodiode. Comparing the light intensity for direct and reflected light allows to determine the absolute mirror reflectivity as function of incident wavelength,  $\lambda$ , in the range between 180 nm and 800 nm with an accuracy of about 2%. Figure 1 shows our results, indicated with WU. They are compared to measurements, which were performed in cooperation with Andre Braem from CERN [3] for the *Compas*- and *Flabeg*-mirrors and to measurements from *JLO Olomouc* [4], which extend to wavelengths below 200 nm.

Samples from *JLO Olomouc* and *Flabeg* show very good reflectivity between 80% and 90%. The *JLO Olomouc* shows slightly better results in the short wavelength range, where most of the Cherenkov photons are emitted. The reflectivity of the *Compas* mirror sample lies at about 75% at  $\lambda > 250$  nm and drops even below 70% at  $\lambda < 250$  nm.

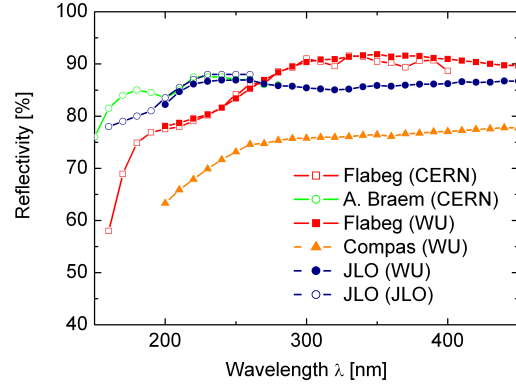


**Figure 1.** Measured reflectivity of mirrors from three manufacturers. Measurements were carried out at the Wuppertal University, at CERN and in the laboratories of *JLO Olomouc*.

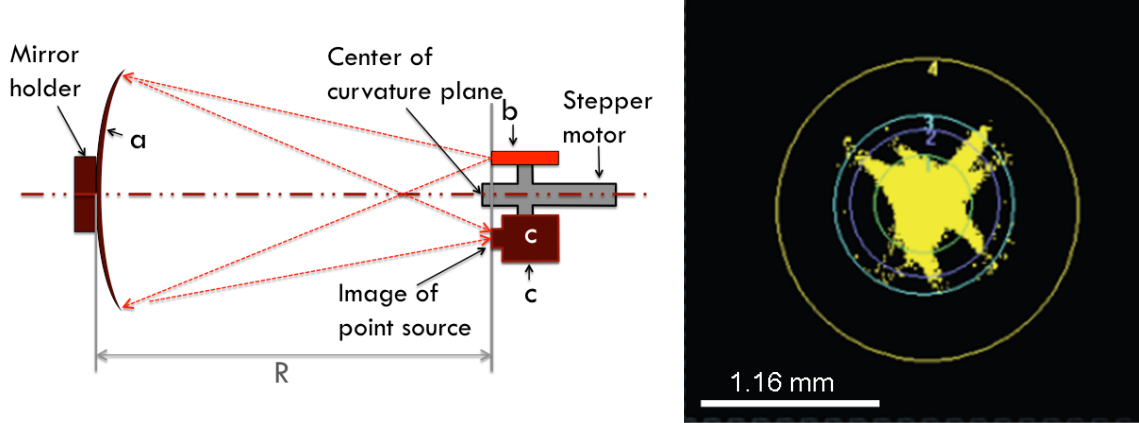


**Figure 2.** Left: Experimental setup for  $D_0$  measurements. Right: Typical image of reflected light on the chip of the CCD camera.

**Surface homogeneity.** The mirror surface homogeneity is characterized by the  $D_0$  quantity.  $D_0$  is the diameter of the circle, which contains 95% of the reflected light in the projected image of a point-like source being located in the focal point of the mirror.

The left panel of figure 2 shows a sketch of the experimental setup being used to measure  $D_0$ . It consists of the test-mirror (a) and a CCD camera (b) with close-by laser driven isotropic point source (c), which illuminates the whole mirror. The CCD camera and the isotropic point source are located exactly in the focal distance of the mirror such that the projected image of the point source is centered on the CCD sensor.

Ideally the image of the reflected light on the camera chip is point like. In reality it is a non homogeneous spot due to deviations and deformations of the mirror surface caused by the manufacturing processes (such as polishing and cutting). The right panel of figure 2 shows an example of a recorded image of the spot on the chip of the CCD camera. Results from *Flabeg* show a confused image and a very large (not measurable)  $D_0$ . Samples from *JLO Olomouc* and *Compas* show low  $D_0$  values of about 2.3 mm. These values are within our tolerances, since taking the resolution of MAPMTs into account (pixel size of 6.5 mm), the CBM-RICH can easily tolerate a  $D_0$  of 3 mm.

Results on reflectivity and surface homogeneity obviously favor the *JLO Olomouc* mirrors.

## 2.5 Photon detector

For the readout of the CBM-RICH detector we presently study different alternatives based on flat-panel Multi-Anode Photomultipliers (MAPMTs) or multichannel Microchannel Plates (MCP-PMTs). The latter are of interest in particular due to their good magnetic field resistivity. The following devices were tested in detail in the lab and in beam tests:

**Hamamatsu H8500** The size of the H8500 type MAPMT is 52 mm  $\times$  52 mm (2" square tube) with 8  $\times$  8 pixel. For the window UV-extended borosilicate glass is used coated with a bialkali cathode (BA). By default we use the version with 12 dynode stages but we also tested versions with Superbialkali cathode (SBA) and 8 dynode stages (H10966).

**Hamamatsu R11265** The R11265 MAPMT is a smaller 1" square MAPMT, with a size of 26 mm  $\times$  26 mm and 4  $\times$  4 pixel (pixel size itself is similar to the H8500). The window also consists of UV-extended borosilicate glass, but this tube is available with a Superbialkali cathode. This type is the recommended solution by Hamamatsu for single-photon measurements.

**Photonis XP85012** The MCP has a size of 59 mm  $\times$  59 mm with 8  $\times$  8 pixel. In contrast to the MAPMTs quartz glass is used as window material. The cathode is made of Bialkali. It's main advantages is the high magnet-field resistance (1-2 T) and the very good time resolution ( $< 50$  ps).

## 2.6 Wavelength range of accessible photons

In general we can state that the chosen detector components work well together in terms of the covered wavelength ranges:

CO<sub>2</sub> absorbs light with wavelengths below 180 nm. This is also the wavelength scale at which chromatic dispersion becomes sizable. So chromatic dispersion will not affect the RICH performance significantly. The mirror reflectivity is on the 85% level over a large wavelength range with a slight drop in the UV range. The quantum efficiency of bialkali photocathodes peaks at about 350 nm and is still sizable large at 200 nm. Using wavelength shifting films, the quantum efficiency in the UV range might even be enhanced up to 20%.

With this concept and components the detector will measure single photons with wavelengths larger than 180 nm with reasonable efficiency.

## 2.7 Resolution of the Cherenkov angle

Particle identification capabilities are strongly related to Cherenkov angle resolution,  $\sigma_\theta$ . A good angle resolution ensures high reconstruction efficiency and consequently electron to pion separation up to high momenta. Several sources can worsen  $\sigma_\theta$  [5, 6]: multiple scattering, chromatic dispersion, magnetic stray field, mirror quality and mirror misalignment, and pixel size of the photon detectors.

Considering the PMT pixel size of about 6.5 mm  $\times$  6.5 mm, the PMT contribution to  $\sigma_\theta$  is 1 mrad. Similar contribution is caused by chromatic dispersion [6]. The contribution from the mirror quality is even much smaller than that. The main contributions to  $\sigma_\theta$  come from the magnetic stray field  $\sigma_B$  and multiple scattering  $\sigma_{MS}$  both showing a momentum dependence with  $\frac{1}{p}$  [5].

For the given length of 1.7 m of CO<sub>2</sub>,  $\sigma_{MS}$  is 2.2, 0.9, and 0.1 mrad for  $p_{\text{particle}}$  of 0.4, 1, and 8 GeV/c respectively. The integrated magnetic field ( $B_y$  component) in the CBM-RICH is 0.077 Tm along the beam axis. Therefore, tracks with  $p = 0.4$  GeV/c ( $p = 1$  GeV/c) suffer a  $\sigma_B$  of 18 mrad (7.2 mrad), while tracks with  $p = 8$  GeV/c suffer a  $\sigma_B$  of 0.9 mrad only.

The numbers given above show that  $\sigma_{MS}$  and  $\sigma_B$  become large for low momenta. As the threshold for Cherenkov radiation for pions in CO<sub>2</sub> lies at 4.65 GeV/c the total resolution of the Cherenkov angle does not harm the electron-to-pion separation up to momenta of 8 GeV/c.

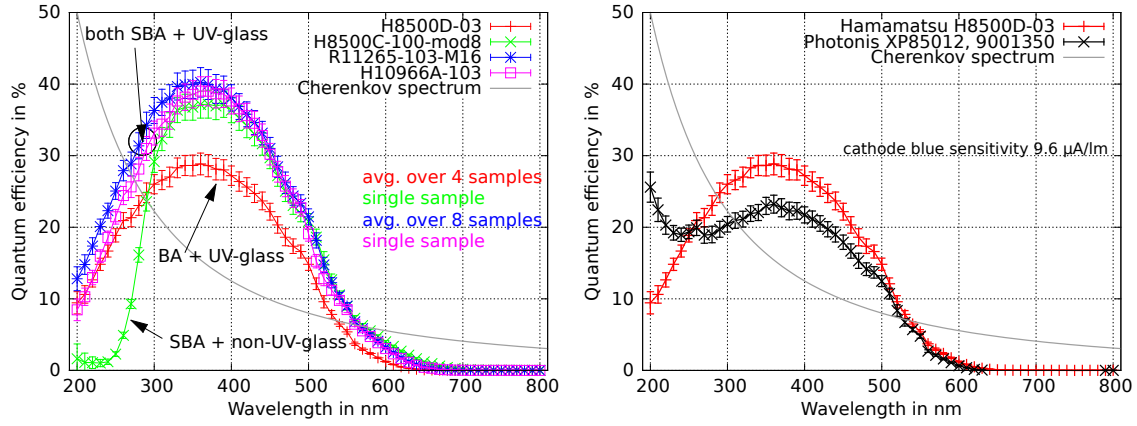


**Figure 3.** Left: Measured quantum efficiencies of several Hamamatsu MAPMTs: H8500D-03 (red; averaged over 4 samples), H8500C-100-mod8 (green; single sample), R11265-103-M16 (blue; averaged over 8 samples), H10966A-103 (purple; single sample). For comparison the Cherenkov-spectrum with  $1/\lambda^2$  is also plotted (gray). Right: Measured quantum efficiencies of 1 sample of Photonis XP85012 MCPs. For comparison the QE of Hamamatsu H8500D-03 MAPMT and the Cherenkov-spectrum are also shown.

### 3 Test results of photon sensor devices

#### 3.1 Quantum efficiency of tested MAPMTs and MCPs

One of the most important characteristics for single-photon detection efficiency is the spectrally resolved quantum efficiency (QE). We measured the quantum efficiency of all these devices in the lab in the wavelength range 200-800 nm, allowing for a detailed comparison, in particular in view of the different cathode materials (BA vs SBA), window materials (UV-glass vs fused silica) and window thicknesses.

Results of these measurements can be seen in figure 3 for tested MAPMTs (left) and for a single MCP (right side).

The measured spectra reveal distinct differences which shall be discussed in more detail: The window material plays an important role in the UV region, standard Borosilicate-windows loose transmittance below 300 nm, where quantum efficiencies of still 10% at 200 nm are possible with UV-glass in case of the tested MAPMTs. The tested MCP, in contrast, shows much higher quantum efficiencies in the UV range thanks to the fused silica window which is unfortunately not available for the MAPMTs due to different thermal expansion coefficients. Quantum efficiency in the UV range is of particular importance due to the  $1/\lambda^2$  spectrum of Cherenkov light.

Comparing peak quantum efficiencies the most striking difference is the significantly increased quantum efficiency of SBA-cathodes in the visible range, with average quantum efficiencies close to 40% at 380 nm for SBA-cathodes on MAPMTs compared to 28% peak values on average for BA-cathodes. However, this increased quantum efficiency in case of SBA nearly vanishes at short wavelengths. This behavior can at least be qualitatively understood by reflectivity measurements of the different photocathode materials as discussed in section 3.2.

The tested MCP reveals slightly lower quantum efficiency in the visible range (23% at 350 nm). For the MAPMTs, figure 3 shows average values over several sample tubes, in case



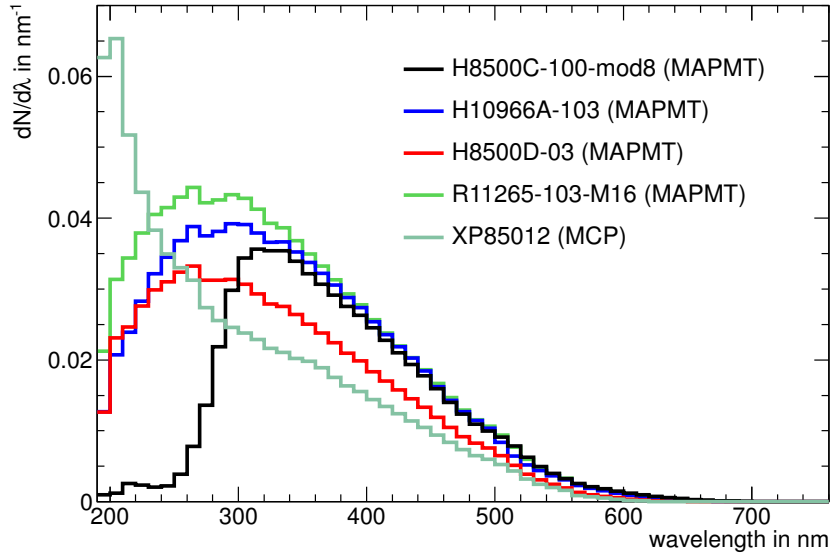


**Figure 4.** Photon yield for all tested devices (quantum efficiency folded with Cherenkov-spectrum) in dependence on wavelength between 200 nm and 800 nm.

of the MCP only a single sample was measured. However, according to the Photonis data sheet, this sample (cathode blue sensitivity of  $9.6 \mu\text{A/lm}$ ) should well reflect the average (typical blue sensitivity  $8.5 \mu\text{A/lm}$ , min.  $7.5 \mu\text{A/lm}$  according to manufacturer specifications).

The slightly increased quantum efficiency of the smaller R11265 tube with SBA-cathode as compared to the 2" H10966 with SBA cathode can be attributed to the reduced window thickness of 0.8 mm (R11265) compared to 1.5 mm (H10966), which influences the transmission capabilities.

In order to obtain a better judgment of the effect of different spectral quantum efficiency curves on the overall Cherenkov photon detection efficiency, we folded the measured distributions with the  $1/\lambda^2$  intensity of Cherenkov light. Results are shown in figure 4. Integrating the total photon yield over the spectrum allows for quantitative comparison of the different photon sensors in terms of expected detection efficiency (assuming similar collection efficiencies for all sensors). Numbers are given in table 1, together with the important properties of each sensor.

As expected from the characteristics of the Cherenkov spectrum the H8500C with borosilicate glass yields the fewest number of detected photons. The difference of BA (H8500D) and SBA (H10966A) is also as expected. And, as mentioned above, the difference of the R11265 and the H10966A (with same window and cathode type) is just a result of the thinner window thickness of the R11265.

One important aspect not included in these studies is the different active area of each sensor type (H8500: 89%, R11265: 77%, XP85012: 80%). The very high geometrical acceptance of the H8500 partially recovers the lower photon yield.

**Table 1.** Important properties of tested MAPMTs and MCPs and the calculated (relative) number of detected Cherenkov photons (by summing up the photon yields shown in figure 4).

MAPMT type	thickness of front glass	window	photo-cathode	no. of dynodes	relative no. of det. Ch. photons
R11265-103-M16	0.8 mm	UV-window	SBA	12	100
H10966A-103	1.5 mm	UV-window	SBA	8	89.7
XP85012	n/a	UV-grade fused silica	BA	MCP	75.7
H8500D-03	1.5 mm	UV-window	BA	12	71.6
H8500C-100-mod8	1.5 mm	borosilicate	SBA	8	62.6

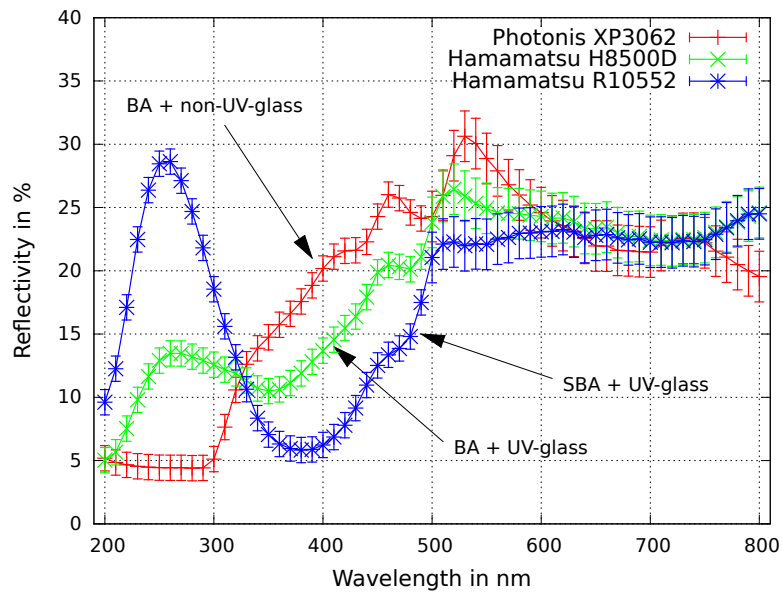


**Figure 5.** Measured specular reflectivities of 3 different PMTs: Photonis XP3062 with BA cathode and non-UV-transparent window (red), Hamamatsu H8500D with BA cathode and UV window (green), Hamamatsu R10552 with SBA and UV window (blue).

### 3.2 QE and reflectivity

As was shown in section 3.1 there is a significant difference in QE between a SBA and a BA cathode in the wavelength region above 300 nm but no difference anymore below 250 nm. One factor which could explain this behavior is the specular reflectivity of the photocathode. Measurements of specular reflectivity of three different PMTs are shown in figure 5.

Especially below 300 nm there is a huge difference between the SBA and the BA cathode, with an highly increased reflectivity of the SBA cathode of nearly a factor of 2. Above 300 nm this effect inverts with a much higher reflectivity of the BA cathode.

When comparing the quantum efficiency and the reflectivity one can conclude, that the higher intrinsic quantum efficiency of the SBA cathode is reduced by the higher reflectivity in the deep-UV region and partially enhanced in the mid-region from 330-500 nm.

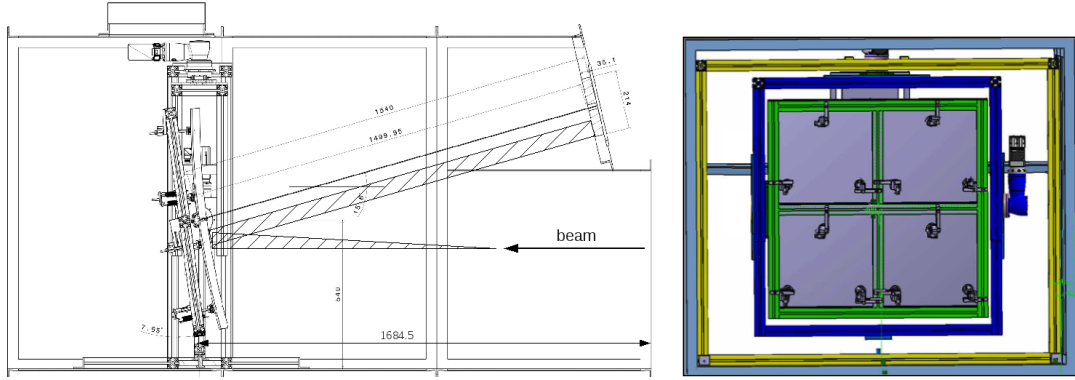


**Figure 6.** Left: Technical drawing of the CBM-RICH prototype box with mirrors on a rotatable frame. The photon detector is mounted on the upper right side. The hatched area visualizes the Cherenkov cone and its reflection onto the photon detector. Right: The mirror system. Each mirror tile is adjustable at three points.

## 4 Real size prototype

### 4.1 Prototype concept

To verify the concept of the CBM-RICH detector a real-size prototype was constructed. It is composed of a gaseous  $\text{CO}_2$  radiator volume, high reflectivity UV mirror tiles and a photon detector composed of MAPMTs and MCP-PMTs, figure 6. The radiator length, the properties and sizes of the mirrors, and the MAPMTs are those currently foreseen for the final CBM-RICH detector.

To ensure a stable and pure  $\text{CO}_2$ -gas supply into the radiator volume, a gas system was build, which keeps the volume under an overpressure of 2 mbar relative to the atmospheric pressure. The gas flow is controlled via a slow control system to stabilize the internal detector pressure by adding more or less fresh pure gas. A purifier and a dryer are part of the system to remove moisture and oxygen from the recirculation flow. The mirror system consists of four mirror tiles of  $(40 \times 40 \text{ cm}^2)$ . Each tile is mounted to a common aluminum frame at three points and can be displaced at these points via remotely operated actuators, compare figure 6. The photon detector consists of several types of MAPMTs and MCPs, see section 2.5.

The prototype concept was implemented in the CBM-Root simulations framework with measured properties of the components ( $\text{CO}_2$  transmittance, mirror reflectivity and the quantum efficiency of the MAPMTs, etc.). The collection efficiency of MAPMTs is set to 100%. Detailed simulations were carried out to determine the performance of the prototype.

In fall 2011 and fall 2012 the prototype was tested at the PS/T9 beam line at CERN. All aspects, which are necessary for a successful operation were tested systematically. Figure 7 shows a typical example of an electron ring with very low noise. The dark rate is found to be below 10 Hz per pixel for the H8500 PMT. The XP85012 MCP and the R11265 PMT show higher rates, which are still tolerable. All simulated and mea-

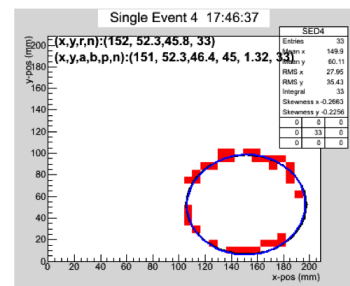


**Figure 7.** Cherenkov ring from a typical single  $3 \text{ GeV}/c$ -electron with a circle fit.

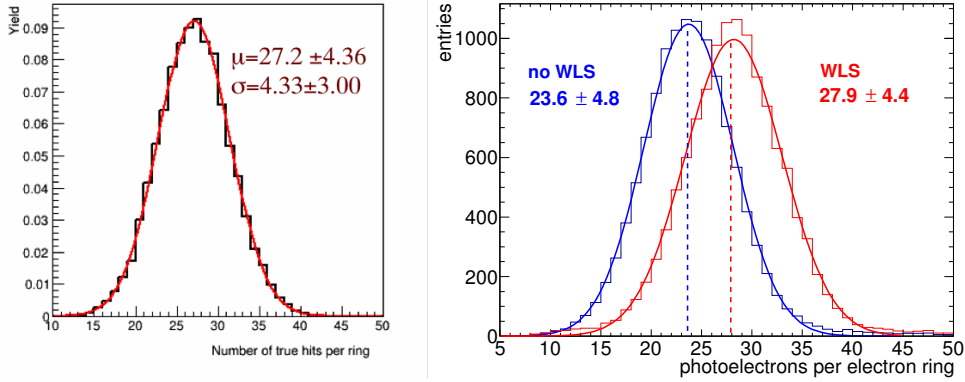


**Figure 8.** Simulated (left, no WLS) and measured (right) number of hits per electron ring in the CBM-RICH prototype. The measured data are corrected for pressure and temperature deviations from the simulation environment. The discrepancy of about 13% between simulations and measurements (blue histogram) can be explained by the collection efficiency of the photon detectors, which is set to 100% in the simulations. The red histogram in the right panel shows the increase of the recorded number of hits per electron ring when utilizing wavelength shifting films.

sured ring properties are in very good agreement. All rings with a number of hits larger than 6 can be found with an efficiency of 100%. The Cherenkov angle resolution is in the order of  $\sigma_\theta = 1.3\%$ . Detailed results of main topics are discussed in the following sections.

## 4.2 Number of hits per ring and ring radius

The left (right) panel of figure 8 shows the simulated (measured) number of hits,  $n_{hits}$ , per electron ring at 3 GeV/c momentum. Simulations are carried out at atmospheric pressure and at zero temperature, whereas the measurements were carried out at a pressure of 0.96 bar and a temperature of 293 K. Due to the dependence of the refractive index on pressure and temperature, the measured data have to be corrected. After the correction the simulated number of hits per ring of  $n_{hits} = 27.2$  is about 13% higher than the measured  $n_{hits}$  of about 23.6 (blue histogram). This discrepancy can be explained by the collection efficiency of the MAPMTs, which is set to 100% in the simulations.

As mentioned above  $\text{CO}_2$  is transparent to photons in the UV range, where most of the Cherenkov radiation is emitted. To increase the integral quantum efficiency of the photon sensors wavelength shifting (WLS) films are investigated. WLS films absorb UV photons and re-emit photons at larger wavelengths where the quantum efficiency of common photocathodes is higher [7]. Simulation and measured data show indeed an increase in  $n_{hits}$  when using p-terphenyl as WLS film as can be seen in the right panel of figure 8, where measured hit multiplicity distributions are shown for coated and non-coated MAPMTs of type Hamamatsu H8500 (2", BA photocathode, and UV-extended window), compare section 2.5. All MAPMT types show such behaviour with a gain in  $n_{hits}$  in the order of 20%.

Each ring is fitted with a circle and an ellipse, figure 7. A simulated radius distribution of the circle fit is shown in the left panel of figure 9 for electrons and pions with a momentum of 8 GeV/c. It is compared to the distribution of the half major axis of the ellipse-fit (called a-axis). The mean

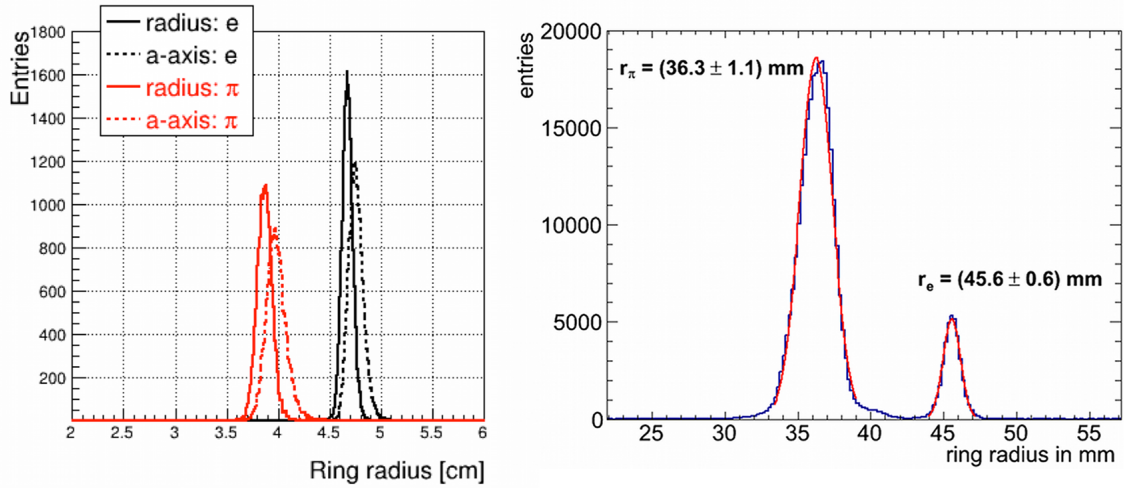


**Figure 9.** Simulated (left) and measured (right) ring radii stemming from electrons and pions. When corrected for temperature and pressure deviations, both agree very well.

values of the electron ring radius and the a-axis are 4.68 cm and 4.78 cm respectively. The mean values of the radii and the a-axis stemming from the pions are 3.88 cm and 4.01 cm respectively.

The right panel of figure 9 shows the measured ring radius distribution of Cherenkov rings stemming from electrons (4.56 cm) and pions (3.63 cm). The deviation of about 5% from simulated data is due to differences in pressure and temperature. When correcting for that the results are well in line with simulations.

To quantify the electron-pion separation capability of the prototype detector, we define a pion identification efficiency,  $\pi_{\text{eff}}$ , by setting the electron identification efficiency,  $e_{\text{eff}}$ , to 95%. i.e 95% of all electrons are identified correctly. The electrons corresponding to this ratio lie within a window of  $\pm k\sigma$  around  $\mu$ , where  $\sigma$  and  $\mu$  are the width and the mean value of a Gaussian fit to the electrons distribution. The factor  $k$  varies slightly depending on the particle momentum under consideration; typical values are around 2.  $\pi_{\text{eff}}$  is then defined as the ratio of pions lying in the  $\mu \pm k\sigma$  window to all pions. The ratio  $R_{\pi/e} = 1/\pi_{\text{eff}}$  is the so called pion suppression factor: For an electron efficiency of  $e_{\text{eff}} = 95\%$ , one pion out of  $R_{\pi/e}$  is then misidentified as electron.

$\pi_{\text{eff}}$  is calculated from the data with momenta between 7 GeV/c and 10 GeV/c. The right panel of figure 10 shows  $\pi_{\text{eff}}$  from data and simulations. The error bars show statistical errors only. Within errors simulated results agree very well with measured data and show a low pion efficiency below 0.00025 for all momenta below 10 GeV/c. This indicates the powerful pion suppression capability of the CBM-RICH detector. The discrepancy at 10 GeV/c can be understood from the fact that in data muons are present in the sample but not in simulations.

At momenta lower than 10 GeV/c both pions and muons are well separated from the electrons, while at  $p = 10 \text{ GeV/c}$  the pion tail -containing also residual muons- comes close to the electron distribution resulting in more non-electrons within the electron window leading to a higher pion efficiency.

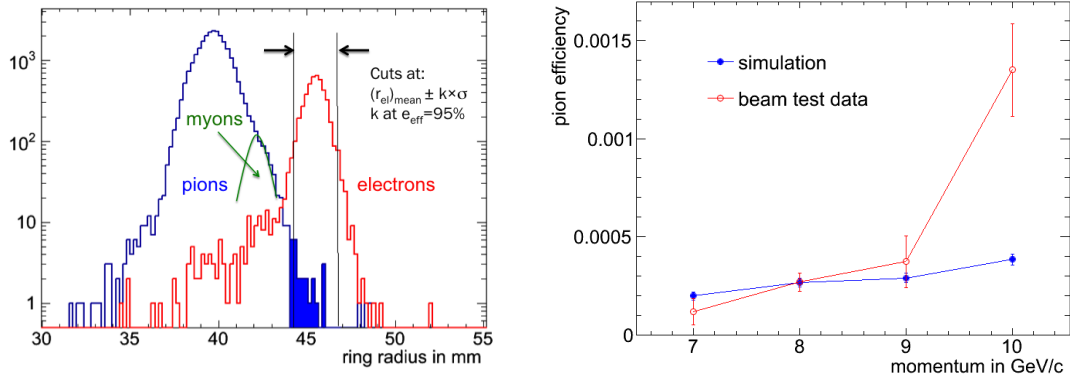


**Figure 10.** Left: Ring radius distribution of pions, muons, and electrons at  $p = 8 \text{ GeV}/c$ . Right: Prototype pion efficiency  $\pi_{\text{eff}}$  from simulation (black line) and data (red line) at an electron identification efficiency of 95%. Error bars show statistical errors.

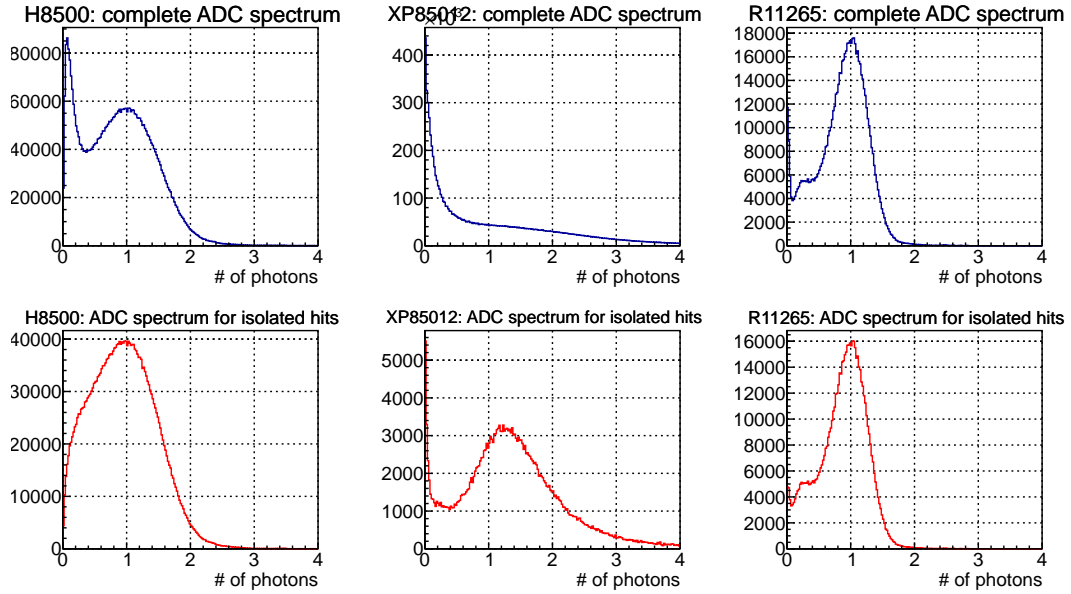


**Figure 11.** Measured ADC spectra of all hits (top) and for isolated hits only (bottom) for one H8500 PMT (left), one XP85012 MCP (mid) and one R11265 PMT (right).

### 4.3 Comparison of single photon spectra

Distinct single-photon peak and good peak-to-valley ratios are important quality criteria to compare different sensor devices. A distinct single-photon peak allows for easy threshold adjustment and good photon detection efficiency in sensor operation.

Figure 11 compares single-photon spectra for three different sensor candidates: The H8500 MAPMT (left column), the XP85012 MCP-PMT (middle column), and the R11265 MAPMT (right column). All spectra show the sum of all 64 (16 in case of R11265) channels after individual channel-by-channel gain normalization. The upper row of the presented spectra is obtained without

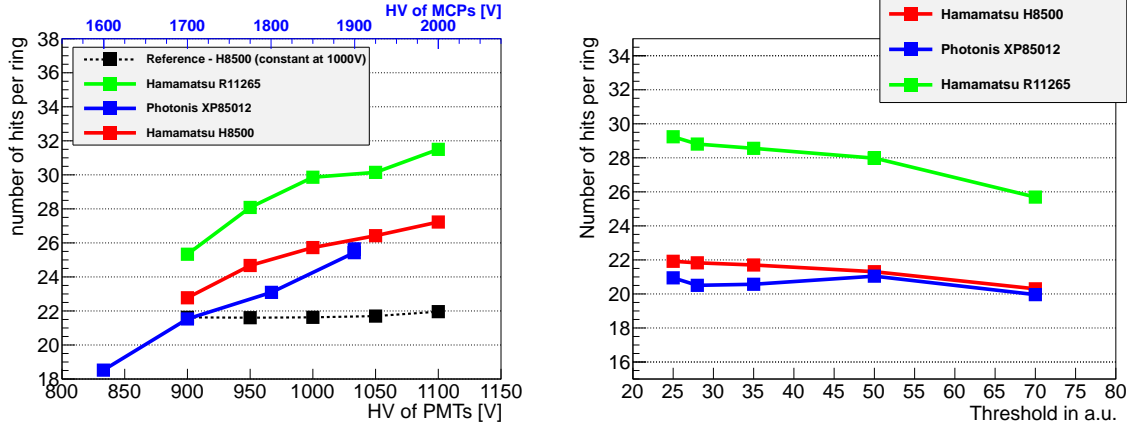


**Figure 12.** Left: Number of hits per Cherenkov ring for various HV-values with fixed hardware threshold. Shown are the values including corrections (geometrical coverage, pressure/temperature, crosstalk). The axes are arranged, such that the standard HV (1000 V for PMTs, 1850 V for MCPs) is at the same point. Right: Number of hits per Cherenkov ring for various hardware threshold-values with fixed (standard) HV. Shown are only the values with corrections.

further cuts, the lower row of spectra shows the ADC response excluding all hits with additional hit entries in neighboring channels. The latter condition effectively suppresses the low amplitude exponential part of the spectrum which is caused by charge sharing between neighboring channels. We would like to emphasize here, that this low amplitude peak, which can be suppressed with this additional cut, is no pedestal peak and not caused by noise.

The low amplitude peak is most dominantly seen in the MCP spectra, an indication for much larger low-amplitude crosstalk observed for the MCPs as compared to the PMTs. Also the H8500 MAPMTs show a distinct amount of low-amplitude crosstalk from neighboring channels, where the smaller R11265 MAPMT shows hardly any difference between upper and lower spectrum due to better channel separation in the dynode system, and larger fraction of edge-pixels (with less neighbors) due to the lower pixel number.

In conclusion, the R11265 MAPMT shows clearly the most favorable single-photon response with a clearly separated and comparatively narrow single-photon peak.

#### 4.4 Performance of MAPMTs/MCPs: Cherenkov ring hit multiplicity

For a qualitative evaluation of the different sensor types Cherenkov data sets with varying high voltage (with fixed threshold) and hardware threshold (with fixed HV) were taken. From these data sets the (mean) number of hits per Cherenkov ring was extracted and corrected for their geometrical coverage (to be able to compare all sensor types), for the difference in temperature and pressure and for the crosstalk behavior.

The resulting number of detected Cherenkov photons for the three sensor types can be seen in figure 12 (left for varying HV and right for varying hardware threshold).

From both measurements the conclusion is that the R11265 PMT shows the best performance, clearly better than the H8500 PMT, as expected from the increased quantum efficiency of the SBA



photocathode. The H8500 MAPMT and the XP85012 MCP show similar Cherenkov detection efficiencies, with about 25% less detected photons per Cherenkov rings compared to the R11265.

#### 4.5 Further detector aspects evaluated in the beam tests

**Radiator contamination.** The gas system provides pure CO<sub>2</sub> and keeps the prototype under an overpressure of 2 mbar relative to the atmospheric pressure. During both beam times the system worked very stably and could keep the RICH gas box under the anticipated pressure. As for the gas contamination, mainly oxygen and moisture, the system works sufficiently well and reduces them to 100 ppm and 280 ppm respectively. To determine contamination tolerances the radiator gas was artificially contaminated with air. The measured oxygen and moisture levels have been increased to 1% for oxygen and 1100 ppm for moisture. Even this high contamination level does not affect the measured number of photons per ring and the ring radius.

**Mirror displacements.** When constructing the mirror plane of the RICH detector, misalignment between the mirror tiles relative to each other and to the nominal common spherical surface cannot be completely avoided. Such misalignment leads to displacements of a mirror tile along the  $z$ -axis at one or more of its sides, which results in displacing the hit position of a reflected photon on the detector plane. This can corrupt the shape and properties, mainly resolution, of Cherenkov rings that are partially reflected at displaced mirrors.

A displacement of the mirror at any of its sides,  $\Delta z_{\text{Rot}}$ , corresponds to a rotation of it around the axis running along its opposite side by an angle  $\alpha_{\text{Rot}}$ . To determine displacement tolerances on  $\Delta z_{\text{Rot}}$  ( $\alpha_{\text{Rot}}$ ) detailed simulations and measurements were carried out taking all potential displacements into account, also in combinations. The results show that displacement at any mirror side can be tolerated up to  $\Delta z_{\text{Rot}} = 0.32$  mm, corresponding to an angle of  $\alpha_{\text{Rot}} = 1$  mrad.

### 5 Conclusion

To achieve electron identification up to  $p = 8$  GeV/ $c$  in the CBM experiment, a RICH concept has been established with three main components: CO<sub>2</sub> as radiator gas, spherical glass mirrors with a reflective Al+MgF<sub>2</sub> coating, and MAPMTs as photon detector. Several types of mirrors and MAPMTs were tested in the lab for their relevant properties.

The RICH concept could successfully be confirmed by intensive and detailed studies including simulations and measurements with a laterally scaled prototype. Measured Cherenkov rings could be recorded and fitted at the level of 100%. The data show a high pion suppression performance of the detector up to  $p = 8$  GeV/ $c$ .

### Acknowledgments

This work was supported by the Hessian LOEWE initiative through the Helmholtz International Center for FAIR (HIC for FAIR) and the German Federal Ministry for Education and Research (Bundesministerium für Bildung und Forschung (BMBF)). We also thank Christian Joram and André Braem from CERN for valuable support in mirror measurements and first evaluation of the WLS effect.



## References

- [1] C. Höhne, F. Rami and P. Staszal, *The Compressed Baryonic Matter Experiment at FAIR*, *Nucl. Phys. News* **310** (2006) 19.
- [2] H. Morii et al., *Quenching Effects in Nitrogen Gas Scintillation*, *Nucl. Instrum. Meth. A* **526** (2004) 399.
- [3] A. Braem, private communication.
- [4] P. Schovanek et al., *Mirror segments for large mirror systems of weak optical signal detectors for UV spectral range*, *Proc. SPIE* **8126** (2011) 812619.
- [5] T. Ypsilantis and J. Seguinot, *Theory of ring imaging Cherenkov counters*, *Nucl. Instrum. Meth. A* **343** (1994) 30.
- [6] P. Glässel, *The limits of the ring image Cherenkov technique*, *Nucl. Instrum. Meth. A* **433** (1999) 17.
- [7] C. Hohne et al., *Development of a RICH detector for CBM: Simulations and experimental tests*, *Nucl. Instrum. Meth. A* **639** (2011) 294.